ADVANCED MATERIALS
www.advmat.de

Pseudotunnel Magnetoresistance in Twisted van der Waals Fe_3GeTe_2 Homojunctions

*Reiji Obata, Haiming Sun, Kartik Samanta, Naafis Ahnaf Shahed, Mioko Kosugi, Takashi Kikkawa, Alaa Abdallah, Kenji Watanabe, Takashi Taniguchi, Kazu Suenaga, Eiji Saitoh, Shigeo Maruyama, Kazuhiko Hirakawa, Kirill D. Belashchenko, Evgeny Y. Tsymbal, and Junji Haruyama**

Twistronics, a novel engineering approach involving the alignment of van der Waals (vdW) integrated two-dimensional materials at specific angles, has recently attracted significant attention. Novel nontrivial phenomena have been demonstrated in twisted vdW junctions (the so-called magic angle), such as unconventional superconductivity, topological phases, and magnetism. However, there have been only few reports on integrated vdW layers with large twist angles θ_t, such as twisted interfacial Josephson junctions using high-temperature superconductors. Herein, vdW homojunctions of the thin-magnetic flakes, Fe_3GeTe_2 (FGT), with large θ_t ranging from 0° to 90°, without inserting any tunnel barriers are assembled. Nevertheless, these vdW homojunctions exhibit tunnel-magnetoresistance (TMR) like behavior (pseudo-TMR (PTMR) effect) with the ratios highly sensitive to the θ_t values, revealing that the vdW gap at the junction interface between the twisted FGT layers behaves like a tunnel barrier and the θ_t serves a control parameter for PTMR by drastically varying magnitudes of the lattice-mismatch and the subsequent appearance of antiferromagnetic (AFM) spin alignment. First-principles calculations considering vacuum gaps indicate strong dependence of TMR on the θ_t driven by the sixfold screw rotational symmetry of bulk FGT. The present homojunctions hold promise as a platform for novel AFM spin-dependent phenomena and spintronic applications.

1. Introduction

Twistronics, an innovative engineering method involving the alignment of van der Waals (vdW) integrated two-dimensional (2D) material layers at specific orientations and angles, has achieved tremendous success in controlling the charge, orbital, and spin degrees of freedom, resulting in various attractive and nontrivial phenomena. Among them are unconventional superconductivity,[1–4] topological phases with strong electron correlations (Chern insulators),[5–7] and magnetism.[8–10] Most of these phenomena arise from Moiré superlattices formed by small rotational misalignment (i.e., via. the so-called magic angle) and lattice mismatch, which may introduce the interplay between the band structure and topology, electron–electron interactions, and atomic reconstructions. Moiré superlattices are created mainly by vdW integration of various 2D layers following a stamp method, while recent works have

R. Obata, M. Kosugi, A. Abdallah, J. Haruyama
Faculty of Science and Engineering
Aoyama Gakuin University
5-10-1 Fuchinobe, Sagamihara, Kanagawa 252-5258, Japan
E-mail: J-haru@ee.aoyama.ac.jp

H. Sun, K. Suenaga
The Institute of Scientific and Industrial Research
Osaka University
Mihogaoka 8-1, Ibaraki, Osaka 567-0047, Japan

K. Samanta, N. A. Shahed, E. Saitoh, K. D. Belashchenko, E. Y. Tsymbal
Department of Physics and Astronomy & Nebraska Center for Materials and Nanoscience
University of Nebraska
Lincoln, NE, USA, 68588

T. Kikkawa
Department of Applied Physics
The University of Tokyo
7-3-1 Hongo Bunkyo-ku, Tokyo 113-8656, Japan

K. Watanabe
Research Center for Electronic and Optical Materials
National Institute for Materials Science
1-1 Namiki, Tsukuba 305-0044, Japan

T. Taniguchi
Research Center for Materials Nanoarchitectonics
National Institute for Materials Science
1-1 Namiki, Tsukuba 305-0044, Japan

E. Saitoh
Institute for AI and Beyond
The University of Tokyo
7-3-1 Hongo, Bunkyo-ku, Tokyo 113-8656, Japan

The ORCID identification number(s) for the author(s) of this article can be found under https://doi.org/10.1002/adma.202411459

DOI: 10.1002/adma.202411459

reported successful formation of Moiré superlattices by precise crystal growth using chemical vapor deposition (CVD), such as twisted bilayer-MoS_2[11] and WS_2[12] with wide twist angles from 0° to 120°.

In contrast, there have been only few reports on integrated vdW layers with large twist angles θ_t.[13–16] Twisted interfacial Josephson junctions between $Bi_2Sr_2CaCu_2O_{8+x}$ superconductors, where superconducting CuO_2 homojunctions are Josephson-coupled through insulating SrO-BiO heterojunctions, have attracted interest to large-θ_t twistronics.[15] It was revealed that the critical Josephson current was suppressed by two orders of magnitude close to $\theta_t = 45°$ due to the complete mismatch of the nodal superconducting order parameters, presenting a chiral topological phase (i.e., two gapless, topologically protected chiral edge modes per monolayer).[14]

In the context of magnetism,[17] exfoliated vdW layers of Fe_3GeTe_2 (FGT) have recently garnered significant attention due to their interesting 2D magnetic properties. Among them are gate-tunable Curie temperature,[18,19] interlayer coupling,[20] and magnetic skyrmions.[21–23] While FGT is predominantly ferromagnetic (FM), the manifestation of antiferromagnetism has been reported.[24–28] Notably, FGT layers have been revealed to be versatile as electrodes in vdW magnetic tunnel junctions (MTJs) and giant magnetoresistance (GMR) devices.[29–34] Density functional theory (DFT) calculations of spin-dependent electronic transport across vdW MTJs (with graphene, monolayer hexagonal boron nitride (hBN), or vacuum tunnel barriers) predicted possibilities for giant tunnel-magnetoresistance (TMR) effects (>1000%) driven by the spin-polarized electronic structure of FGT.[29] A TMR ratio as large as ≈300% was experimentally confirmed in spin valves utilizing FGT/hBN/FGT vdW MTJs.[30] Employing vdW semiconductor spacer layers instead of insulator spacers has also allowed high TMR ratios (≈200%).[30,4]

Similar to other vdW materials, thin FGT layers can be assembled in a twisted homojunction. Experimentally, it was demonstrated that two thin twisted FGT layers with $\theta_t \approx 90°$ exhibited a plateau-like MR with a small ratio of ≈0.07% due to the anti-FM (AFM) spin alignment of the FGT layers.[35] Theoretically, it was predicted that FGT homojunctions with twist angles $\theta_t = 0°$ and 180° had different interlayer magnetic orderings due to changes in the electronic structure and charge transfer.[24] Apart from FGT, electron tunneling across magnetic layers of CrI_3 demonstrated a colossal MR effect (≈19 000%) due to the intrinsic AFM coupling between the CrI_3 monolayers and their magnetic alignment being controlled by an applied magnetic field.[36,37] Twisted vdW bilayer CrSBr, an antiferromagnet, also realized a high TMR ratio (≈900%).[38]

These findings suggest that vdW-assembled homojunctions of magnetic FGT layers with large θ_t are promising for novel spin-dependent phenomena and potential applications in lattice-mismatch spintronics. In the present work, we directly assemble thin FGT flakes with large θ_t (from 0° to 90°) into homojunctions without inserting any barrier layers. The TMR-like behavior, which we dub pseudo TMR (PTMR), is observed, exhibiting MR peaks with rectangular top shapes, contingent on the orientation of the magnetic field (B) (or $\pm B$ regions), θ_t, back gate voltage (V_{bg}), and temperature (T). The strongest PTMR of ≈14% is observed at $\theta_t = 45°$ for V_{bg} of +45V in $+B$ region at $T = 2$ K, while disappearing at $\theta_t = 60°$. We argue that under conditions of vdW assembly with observation by cross-sectional scanning transmission electron microscope (CS-STEM), the vdW gap (Δ_g) at the junction interface between two assembled FGT layers is enhanced compared to the bulk material due to the lattice mismatch. This Δ_g serves as a tunneling barrier producing PTMR when their spin alignment changes from FM to AFM by varying applied B. Our DFT calculations demonstrate that PTMR strongly depends on the θ_t values due to the dissimilar momentum-dependent tunneling of majority and minority-spin electrons between the FGT layers across the vacuum gap. The results are in good agreement with the experimental results for the θ_t dependence of PTMR values.

2. Results and Discussion

2.1. Sample Preparation and Characterization

In the current experiments, vdW-integrated and twisted thin FGT flakes with various θ_t are formed following the mechanical exfoliation and stamp methods using the Scotch tapes and polydimethylsiloxane (PDMS) sheets, introducing various θ_t values using a 2D heterostructure transfer system (HQ graphene Co.) (Supporting Information) 1). Each sample is covered by hexagonal boron nitride (hBN) layers. All processes are carried out in a glovebox with Ar-gas atmosphere.

The fundamental properties of the pristine thin FGT flakes are shown in **Figure 1**. These include crystal structures a,b), T-dependence of c) magnetization (M) and d) Hall resistance (R_{xy}), e) magnetization curve and f) Hall-pattern measurement on change in perpendicular magnetic field (B). The Curie temperature $T_C \approx 270$ K and anomalous Hall resistance below 250 K are in good agreement with previous reports,[18,19] as confirmed in Figure 1c,d, respectively. The magnetization curve and Hall-pattern measurement exhibit a conventional M–B curve and an anomalous Hall effect (AHE), which align closely with those previously reported in FGT layers,[18,19] respectively (e) and f)). One significant difference is that the AHE has strong V_{bg} dependence, resulting a stronger response in the positive V_{bg} region in Figure 1f.

Examples of an optical microscope image of the vdW-integrated and twisted two-different thin FGT flakes with theθ_t of 45° is shown in **Figure 2**a with two-probe Au/Ti electrodes (Supporting Information 1). hBN covers all parts of the FGT

E. Saitoh
WPI Advanced Institute for Materials Research
Tohoku University
2-1-1 Katahira, Aoba-ku, Sendai 980-8577, Japan
E. Saitoh
Advanced Science Research Center
Japan Atomic Energy Agency
2-4 Shirakata, Tokai-mura, Naka-gun, Ibaraki 319-1195, Japan
S. Maruyama
Department of Mechanical Engineering
The University of Tokyo
7-3-1 Hongo, Bunkyo-ku, Tokyo 113-8656, Japan
K. Hirakawa, J. Haruyama
Institute for Industrial Sciences
The University of Tokyo
4-6-1 Komaba Meguro-ku, Tokyo 153-8505, Japan

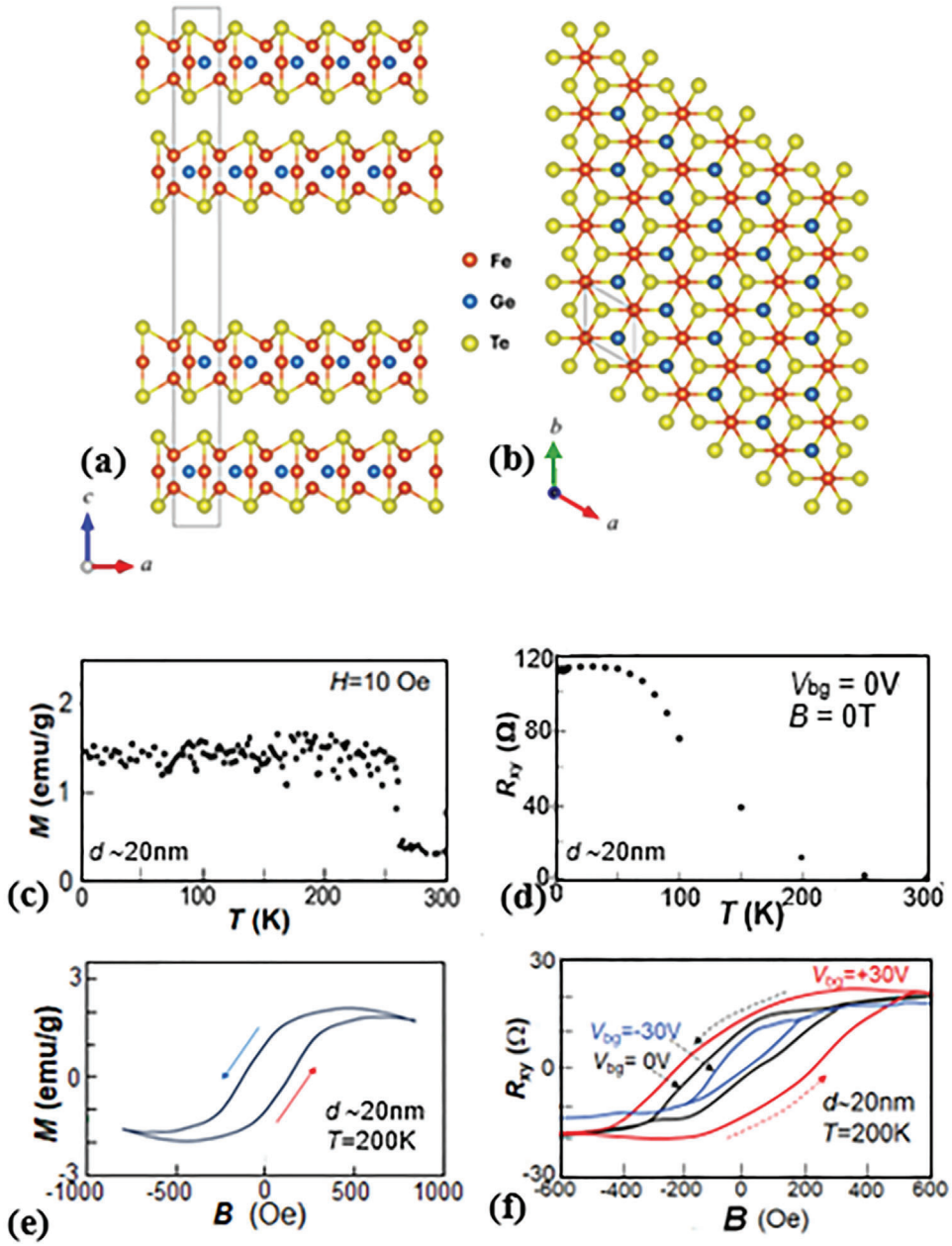

Figure 1. Basic properties of the non-vdW integrated single thin FGT flakes. Atomic structure of an untwisted MTJ where two FGT electrodes separated by vacuum layer of 6 Å added to van der Waal layer separation: a) side view; b) top view. The supercell which is used in the calculation of the scattering region is indicated by the solid line. *T*-dependence of c) magnetization (*M*) and d) Hall resistance (R_{xy}). e) Magnetization curve and f) Hall-pattern measurement for change in perpendicular magnetic fields (*B*)), with V_{bg} dependence in (f).

flakes. An atomic-force microscopy top-view image around the junction part of a) is shown in Figure 2b. The junction area is evident. A cross-sectional atomic force microscopy image of the junction part shown by white dotted line in (b) is presented in Figure 2c. Thickness of each thin layers is confirmed to be ≈20–27 nm.

Examples of CS-STEM images are presented for the upper layer with θ_t of 45° and the lower layers θ_t of 0° in Figure 2d, with the simulation images of 45°- and 0°-tilting relative to [100] orientation (Figure 2e) corresponding to the panel (d). In panel (d), the lower layer indicates a clear image, while the image becomes indistinct and very ambiguous in the upper layer. This supports presence of the θ_t value ≈45° in the upper layer, because many atoms overlap in this θ_t for the CS direction and individual atoms cannot be evidently confirmed in CS-STEM. Figure 2e supports this interpretation. Higher resolution high-angle annular dark field (HAADF)- and bright field (BF)-CS-STEM images of the lower layers along [100] orientation are presented in Figure 2f,g, respectively. Each atom component (corresponding to Figure 1b) can be evidently confirmed in these images.

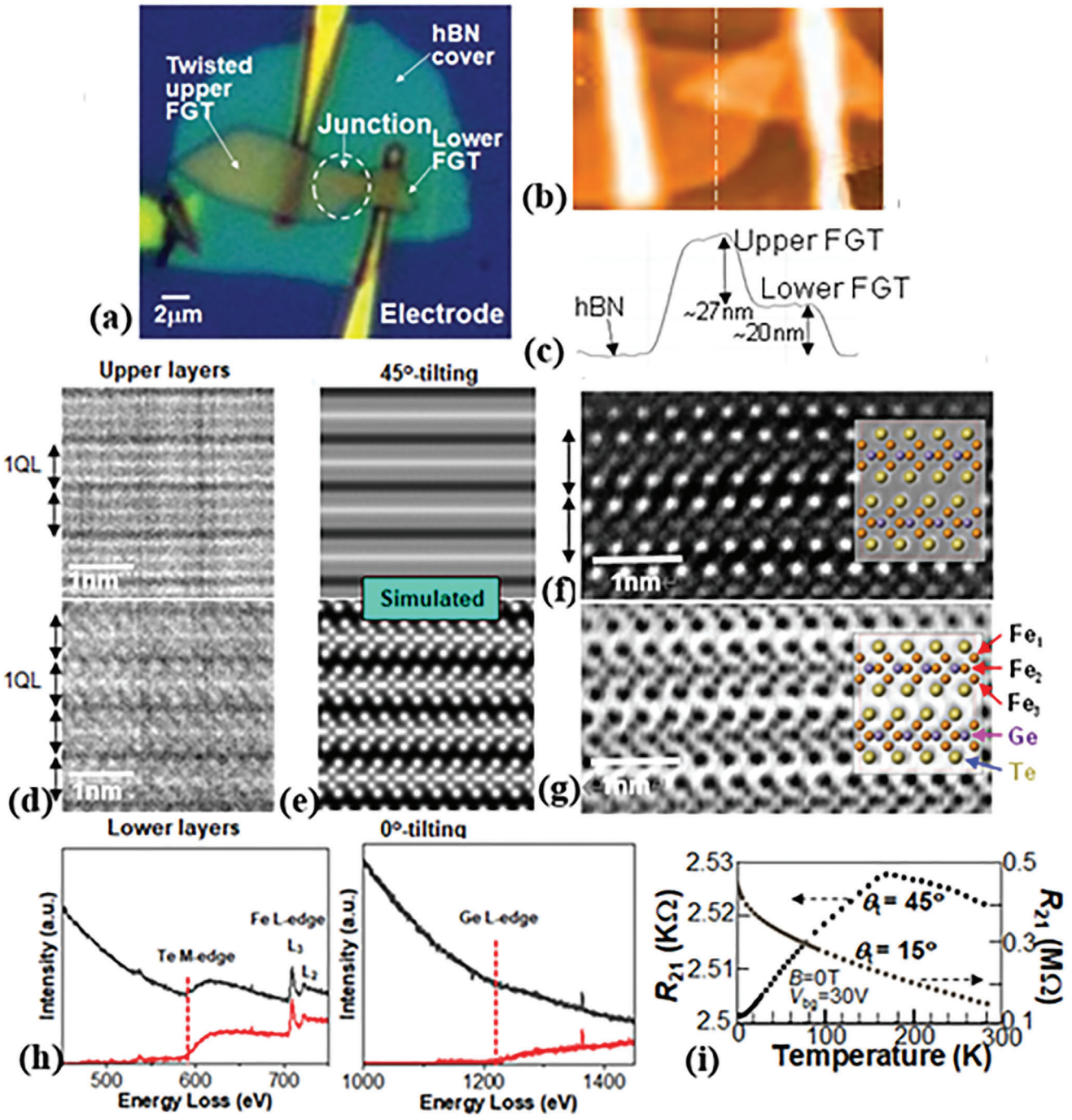

Figure 2. Basic properties of the largely twisted and vdW-integrated thin FGT flakes. a) An optical microscope image of the sample with θ_t of 45° featuring preformed two-probe Au/Ti electrodes. b) Top-view and c) cross-sectional atomic-force-microscopy images around the junction part of (a). Panel (c) is observed along the white dotted line in (b). Examples of CS-STEM images for d) the upper layer with θ_t of 45° and the lower layers with θ_t of 0°, e) simulation images of 45°- and 0°-tilting relative to [100] orientation, corresponding to the panel (d), f) HAADF and g) BF CS-STEM images of lower layers along [100] orientation. 1QL means one quantum layer (QL), which includes all atoms of a FGT unit shown in Figure 1a. h) EELS spectrum. The energy region of the EELS system is fixed to a maximum of ≈600 eV. The energy loss of Te-M, Fe-L, and Ge-L edges are evident at ≈570, 710, and 1220 eV, respectively. i) *T*-dependence of the two-terminal resistance values for the samples with θ_t of 15° and 45°. Contact resistances are subtracted.

Electron energy-loss spectroscopy (EELS) also supports presence of each atom (Figure 2h) (Supporting Information 2). *T*-dependence of the two-terminal resistance (*R*) values with θ_t of 15° and 45°is demonstrated in Figure 2i. As *T* decrease, *R* value slightly increases showing a semiconducting behavior, while it monotonically decreases below $T \approx 180$ K demonstrating a metallic behavior in the sample with $\theta_t \approx 45°$. This implies absence of the intentionally formed tunnel barriers in the sample, although a space ≈1 nm between the two integrated flakes (i.e., corresponding to Δ_g) is observed in CS-STEM images (Supporting Information 2). In contrast, *R* value is very high and monotonically increases in the sample with $\theta_t \approx 15°$, indicating semiconducting or insulating behaviors.

2.2. PTMR Behaviors Depending on θ_t, *T*, and V_{bg}

Typical MR curves as a function of magnetic field *B* for the vdW-integrated and twisted samples are presented for seven different θ_t in **Figure 3**. The MR ratio ($\Delta R/R$) at each *B* is normalized by the MR value at $B = -1$T (i.e., $\Delta R/R = [R(B)\text{-}R(B = -1\text{T})]/R(B = -1\text{T})$). Figure 3d, corresponding to $\theta_t = 45°$, represents a clear emergence of two distinct asymmetric peaks, depending on the direction of the change in *B* (i.e., from $-B$ to $+B$ (blue curve) and its reverse (red curve)). Following each substantial and broad negative MR peak, the red curve shows an asymmetric sharp peak (i.e., butterfly-shape peak) in $-B$ region, whereas the blue curve implies a rectangle-like shape MR peak with almost flat line at the top part (indicated by green dotted rectangle; i.e., PTMR behavior), which possesses $\Delta R/R \approx 10\%$, in $+B$ region. The rectangle-like top-shape peaks are highly sensitive to θ_t and the most pronounced in Figure 3d, while they become less discernible at $\theta_t = 30°$ and 90° (Figure 3c,g). Almost no such peaks are confirmed at $\theta_t = 0°$ and 60° showing only the butterfly-shape peaks (Figure 3a,e). $\Delta R/R$ values and ΔB (width of the *B* region for the top-plateau part of the rectangle-like top-shape peak) are presented as a function of θ_t in Figure 3h. The θ_t dependence is much obvious in this figure, implying the highest values at $\theta_t = 45°$.

The *T*-dependence of the MR behavior of the sample with $\theta_t = 45°$ (shown in Figure 3d) is presented in **Figure 4**a,b (Supporting Information 3). Both peaks become ambiguous as *T* increases. The sharp peak (red curve) survives even at $T = 100$ K and entirely disappears at $T = 150$ K. On the other hand, the rectangle-like top-shape curve (blue curve) narrows as *T* increases, remaining almost flat at the top (Figure 4a). The MR ratio as a function of *T* for the blue curve is shown in Figure 4b. It quickly decreases with increasing *T* and saturates above $T \approx 30$ K. The width of the flat top (plateau) part, ΔB, becomes very narrow with increasing *T*, and completely vanishes above $T \approx 50$ K (Figure 4b). The asymmetric *B* positions for emergence of these asymmetric peaks become almost symmetric at $T \approx 20$ K.

The V_{bg}-dependence of MR for the sample with $\theta_t = 45°$ is demonstrated in Figure 4c,d (Supporting Information 4). The red curves with the sharp peak are almost independent of V_{bg}, while the blue curves with the rectangle-like top-shape peak strongly depend on V_{bg}. For $-V_{bg}$ region, they show only an asymmetric butterfly-shape peak similar to the red curves, without the top plateau parts. On the other hand, the rectangle-like top-shape with very small ΔB appears at $V_{bg} = 0$ V. ΔB broadens and the top plateau shape becomes obvious as $+V_{bg}$ increases (Figure 4d), and the rectangle-like top-shape becomes evident above $V_{bg} = +30$ V. Although $\Delta R/R \approx 10\%$ for the blue curve is almost constant at $V_{bg} < +30$ V, both $\Delta R/R$ and ΔB values increase above $V_{bg} = +30$ V, resulting in the highest $\Delta R/R$ value ≈14% at V_{bg} of +45 V (Figure 4d; and Supporting Information 4).

3. Discussion

3.1. Δ_g- and θ_t-Dependent PTMR Effect

Next, we discuss the observed MR properties of the twisted FGT homojunctions that reveal two butterfly-shape and rectangle-like top-shape peaks in the MR curves. The butterfly-shape MR peak has been reported even for nonintegrated single magnetic layer[26,35,39] and was understood by the anisotropic MR effect, the exchange bias effect, and the magnon scattering in the oxidized surface of the FGT layers, which are present in our case. The rectangle-like top-shape MR peaks are the characteristic feature of the present experiments. We attribute them to a PTMR effect, which arises from the large difference in transmission between FM- and AFM-aligned magnetic moments unique to the two thin FGT layers through a Δ_g (insets of Figure 3b–d,f,g).

We argue that the Δ_g between two vdW-assembled FGT layers is enhanced compared to that in the bulk material. This enhancement follows from the "nonoptimal" structural arrangement of the vdW-assembled layers. Independent of the θ_t, displacement and/or twist of adjacent FGT layers with respect to each other lead to the enhanced separation between them compared to the "optimal" structural arrangement in the bulk structure. For example, our DFT calculation shows that the Δ_g between FGT monolayers in the bulk is increased from ≈0.3 to ≈0.36 nm, when one monolayer is rotated by 30° with respect to the other away from the optimal bulk stacking. This occurs due to the nonoptimal stacking of FGT where Te atoms appear atop of each other. A similar effect occurs when one monolayer is shifted in the plane with respect to the other. These results indicate that assembling two FGT monolayers with twisted/shifted lattices are expected to produce an enhanced Δ_g between them.

Our CS-STEM images (Figure S2, Supporting Information), demonstrate that the visible interlayer gap Δ_g is not uniform along the junction interface. This is largely due to the FGT layers not being flat on the sub-nm scale, so that the depth projection of their surfaces is visible in the 2D images at different local separations. Therefore, to qualitatively characterize the interlayer separation and its change with the θ_t, we use the maximum Δ_g values (Δ_{gmax}) observed at different θ_t. As expected, we find from our CS-STEM images that the $\Delta_{gmax} \approx 0.6 - 0.7$ nm for $\theta_t \approx 30°$ and ≈45° (i.e., the lattice mismatched junctions) is larger than the Δ_{gmax} ≈0.4 nm for $\theta_t \approx 0°$ and ≈60° (i.e., the lattice matched junctions) (Figure 3h; and Supporting Information 2).

This enhanced Δ_g between twisted FGT layers behaves like a tunnel barrier in the vdW-assembled FGT homojunctions which

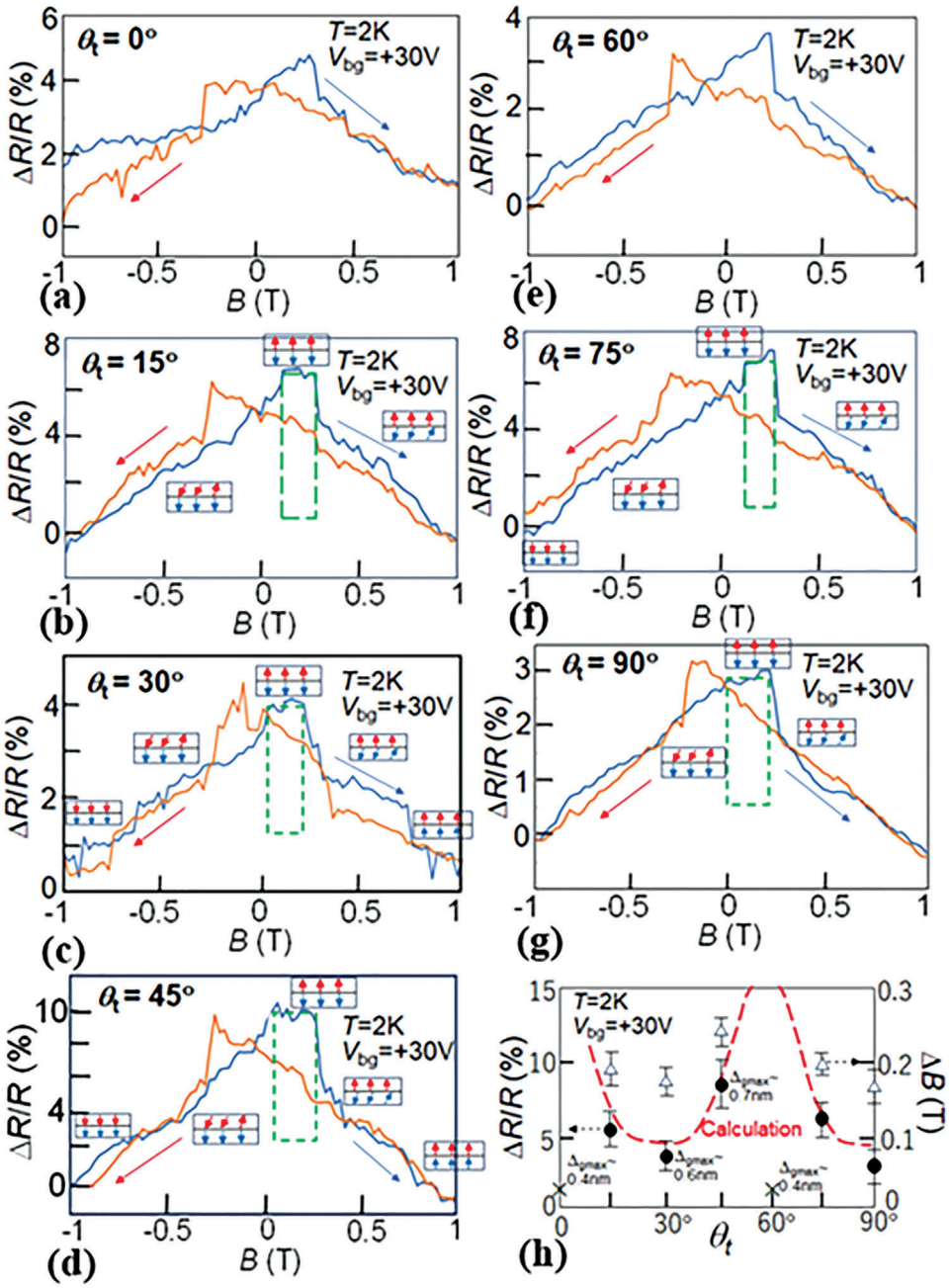

Figure 3. Typical MR behaviors of the vdW integrated and twisted thin FGT samples with each $d \approx 20-30$ nm. a–g) The MR ratio, $\Delta R/R$, as a function of B for seven different θ_t, presenting two distinct asymmetric peaks (i.e., butterfly-shape peak (red and blue curves in (a,e)) and rectangle-like top-shape peaks (blue curves with green dotted rectangle lines for guidance in (b–d,f,g); PTMR behavior)). The value at each B is normalized by the MR value at $B = -1$T (i.e., $\Delta R/R = [R(B)\text{-}R(B{=}-1\text{T})]/R(B{=}-1\text{T})$). Arrows show the direction of the B-change. Fixed current of 1 μA was used for the measurements. Insets in (b–d,f,g): Schematic views of spin alignment in each layer (for blue curves) for different B regions. Arrows mean spin moments. h) $\Delta R/R$ value (filled circle symbols for the left y-axis) and ΔB (width of B region for the top-plateau part; open triangle symbols for the right y-axis) as a function of θ_t for the rectangle-like top-shape peaks (blue curves in (b–d,f,g)) in a few samples (shown by error bars). × symbols mean the absence of the rectangle-like top-shape peak with high reproducibility for four samples. Red-dotted curve is the calculation result shown in Figure 5d. The Δ_{gmax} values (Supporting Information 2) are noted at θ_t of 0°, 30°, 45°, and 60°.

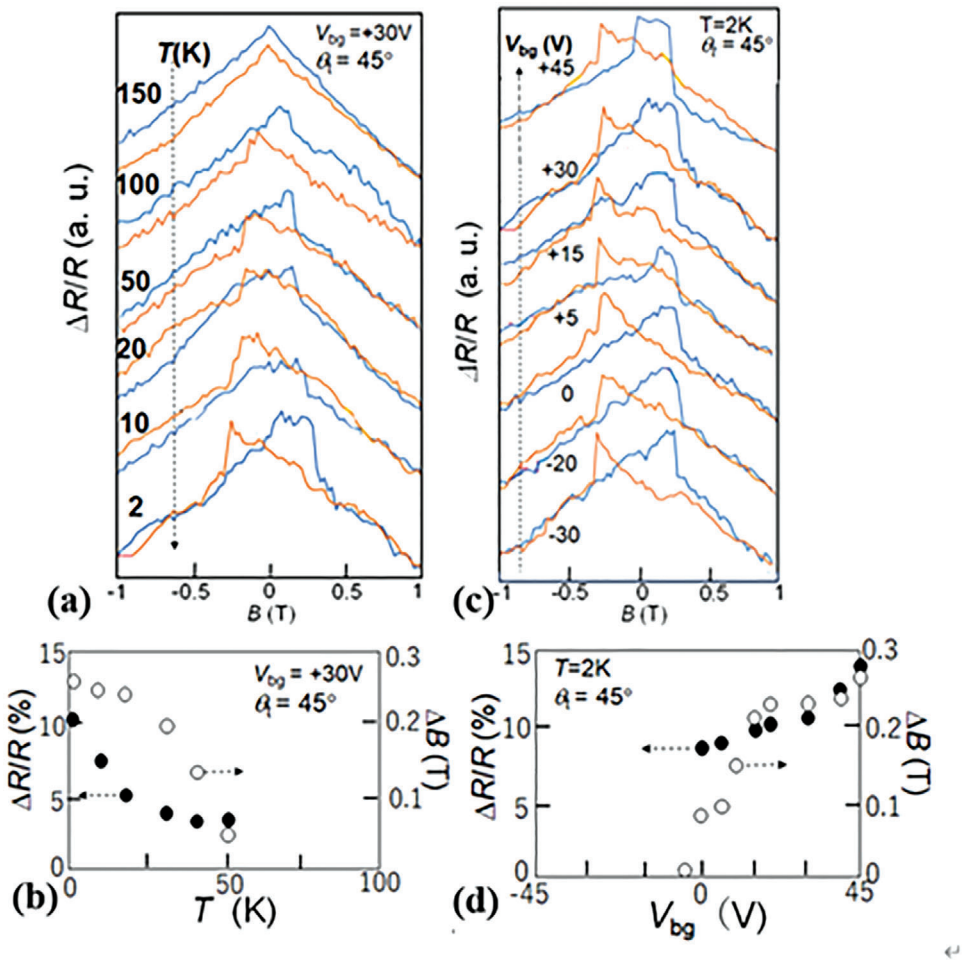

Figure 4. *T*- and V_{bg}-dependence of the MR behaviors of the sample with $\theta_t = 45°$ (shown in Figure 3d). a,c) $\Delta R/R$ as a function of *B* for different *T* a) and V_{bg} c). b,d) $\Delta R/R$ values (black-circle symbols) as a function of *T* b) and V_{bg} d), and ΔB (white circles) versus V_{bg} d) for the rectangle-like top-shape peaks (blue curves in (a) and (c), respectively).

exhibit PTMR with the PTMR ratio changing with the θ_t. The hexagonal lattice structure of bulk FGT has a sixfold screw axis (the *c* axis in Figure 1b). This symmetry is expected to correlate with the measured PTMR of the twisted FGT homojunctions. This correlation may be twofold. First, the PTMR ratio itself is expected to have the 60° periodicity with the twist angle as will be discussed below. Second, the interlayer exchange coupling may also vary with this periodicity. For those angles where the FM interlayer exchange coupling is strong, the AFM alignment between the two FGT layers may not be achieved, thus destroying the PTMR. In fact, the latter case occurs for our samples with $\theta_t \approx 0°$ and ≈60°. As seen from Figure 3a,e, no PTMR plateaus appear in the $\Delta R/R$ versus *B* curves and only butterfly-shape peaks, that are also seen in single FGT layers, are observed. This behavior may be explained by the sixfold rotational symmetry suggesting that the two FGT layers untwisted ($\theta_t = 0°$) or twisted by $\theta_t = 60°$ have bulk-like lattice matching which may favor a stronger FM interlayer coupling. On the contrary, the two FGT layers twisted by $\theta_t = 15°$, 30°, and 45° have a lattice mismatch with respect to the bulk FGT stacking (Supporting Information 5), resulting in a weaker interlayer coupling and thus allowing the formation of the AFM alignment of the magnetization due to different coercivity of the two layers.

3.2. Electron Doping Induced by $+V_{bg}$

Interestingly, the PTMR plateaus become apparent only in the high $+V_{bg}$ region (Figure 4c,d). This observation suggests that electron doping triggered by applying $+V_{bg}$ supports an AFM spin alignment between the twisted FGT layers. This result is closely related to the measured AHE (Figure 1f) whose magnitude becomes larger in the $+V_{bg}$ region. The origin of the V_{bg} dependence of the magnetization is voltage controlled magnetic anisotropy.[40] Applying an electric field to a magnetic film produces an electrostatic doping effect which changes surface (interface) magnetic anisotropy energy. Such an effect has been previously reported in ref. [41] for the case of FGT. This change in the magnetocrystalline anisotropy affects the coercive field and the magnetization of the FGT layer, which we observe in our AHE measurements shown in Figure 1f. These results are consistent with the existing knowledge and previous observations.

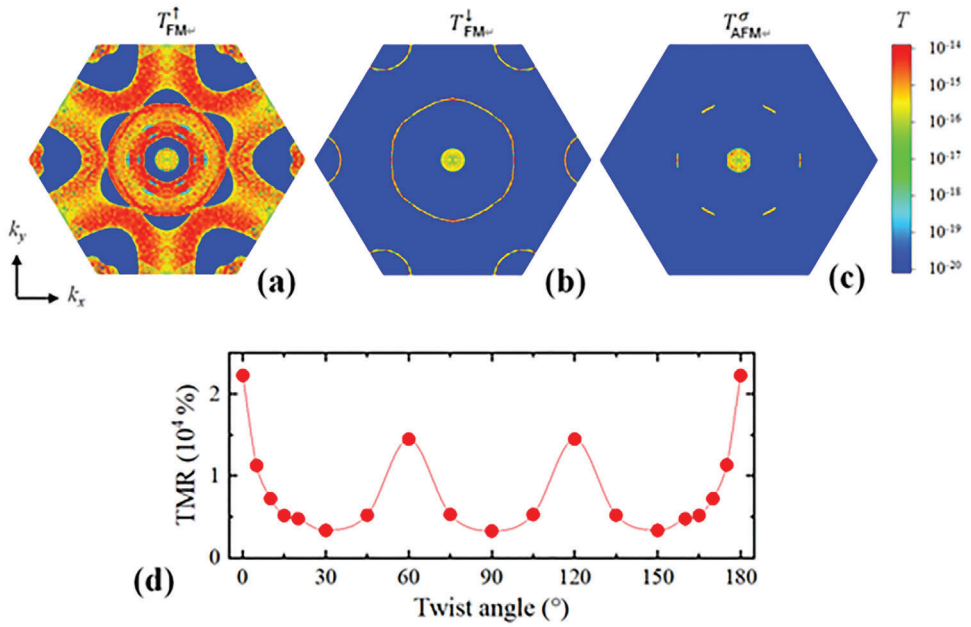

Figure 5. a–c) $k_{\|}$-resolved transmission of a) up- and b) down-spin electrons for FM-aligned MTJ magnetization of the FGT electrodes, $T^{\uparrow}_{FM}$ and $T^{\downarrow}_{FM}$, respectively, and c) AFM-aligned MTJ, T^{σ}_{AFM}, where $\sigma = \uparrow$ or $\downarrow$. d) Calculated TMR ratio of an MTJ with a vacuum barrier layer and two FGT electrodes twisted with respect to each other by θ_t for electron energy $E = E_F$, where E_F is the Fermi energy. Solid lines connecting the dots are just guides for an eye (Supporting Information 6).

3.3. First-Principles Calculations

Due to the Δ_g serving as a barrier layer, the observed PTMR effect can be explained using the mechanism of spin-dependent tunneling that has been previously considered for untwisted FGT-based tunnel junctions.[24] In our case, however, new features of the PTMR effect are expected to occur due to the twist angle affecting the electronic structure of the homojunction. To understand the effect of twist on the tunneling conductance between the FGT layers, we employ a model where the tunneling process in the MTJ is described by matching the true transverse (in-plane) wavevector of vacuum to the quasiwavevectors $k_{\|}$ of the two twisted FGT layers (see Supporting Information 6: Theoretical Model and Computational Methods).

We implement this model for an MTJ which consists of two twisted FGT electrodes separated by a vacuum layer. First, we consider an untwisted MTJ whose atomic structure is shown in Figure 1a,b. We perform quantum-transport calculations of transmission across the MTJ as described in Supporting Information 6. **Figure** 5a–c shows the results for $k_{\|}$-resolved transmission of the majority- and minority-spin electrons for FM-aligned magnetization of the FTG electrodes, $T^{\uparrow}_{FM}(k_{\|})$ and $T^{\downarrow}_{FM}(k_{\|})$, respectively, and AFM magnetization of the FTG electrodes, $T^{\sigma}_{AFM}(k_{\|})$, where $\sigma = \uparrow$ or $\downarrow$. It is seen that, overall, $T^{\uparrow}_{FM}(k_{\|})$ is much larger than both $T^{\downarrow}_{FM}(k_{\|})$ and $T^{\sigma}_{AFM}(k_{\|})$, reflecting the band structure of bulk FGT (Supporting Information 6) where there are many majority-spin conduction channels (i.e., bands crossing the Fermi energy) at different transverse wave vectors, while there are just a few minority-spin conduction channels. As a result, the total conductance for the FM state, T_{FM}, is much larger than the total transmission for the AFM state, T_{AFM}, resulting in the TMR ratio, $TMR = (T_{FM} - T_{AFM})/T_{AFM}$ as large as $\approx 10^4$%. This value is consistent with the previous DFT calculation.[22]

Then, we employ the interface transmission function (ITF)[42,43] and calculate the TMR ratio as a function of θ_t, as described in Supporting Information 6. The results of this calculation are shown in Figure 5d by red dots. The data reveal a strong θ_t-dependence of the TMR exhibiting a quasioscillatory behavior with the highest TMR ratio at $\theta_t = 60°$ and a period of 60°. The calculation result reflects the fact that bulk FGT has a sixfold screw c-axis which is expected to force $k_{\|}$-resolved transmission across bulk FGT to respect this symmetry. The presence of a vacuum layer breaks this symmetry, causing $T^{\sigma}_{FM,AFM}(k_{\|})$ to exhibit a twofold rotational symmetry (see, e.g., Figure 5a where the deviation from the sixfold rotational symmetry in the $T^{\uparrow}_{FM}(k_{\|})$ is most pronounced). Nevertheless, for not too thick vacuum layer, the pronounced features associated with the presence of the sixfold screw axis in the FGT leads are retained and are the origin of the quasioscillatory behavior with a period of 60° seen in Figure 5d.

Compared to our experimental results, we see that while the theory predicts the largest TMR ratios at $\theta_t = 0°$ and 60°, the experiments show the lowest TMR ratios at these angles. This disagreement can be understood by the fact that experimentally at these θ_t, the FGT stacking order is bulk-like, that is, exhibiting a relatively small Δ_g (Supporting Information 2) and strong FM coupling between the FGT layers. Under these conditions, achieving an AFM alignment of the FGT layers is nearly impossible because upon the application of an external B, both FGT layers switch simultaneously. In contrast, at $\theta_t = 30°$ or 45°, the enhanced Δ_g between the FGT layers (Supporting Information 2), on one hand, creates an effective tunnel barrier and, on the other hand, reduces the FM exchange coupling, which makes the AFM

alignment and hence PTMR possible. Indeed, our scaled calculation results (i.e., the quasioscillatory behavior in Figure 5d) are in good agreement with the experimental results except for those at $\theta_t = 0°$ and 60° as shown by red-dotted curve in Figure 3h.

3.4. Factors Preventing High PTMR Ratios

It is noteworthy that the predicted TMR ratios (≈10^4%) are ≈1000-times larger than the PTMR ratios observed experimentally (≈10%). There are several possible reasons for this discrepancy. The primary cause is likely the exchange coupling between the FGT layers which is ignored in the theoretical calculations assuming a perfect FM or AFM alignment of the two layers. As a result, the calculation leads to extremely large TMR values for any θ_t values due to the spin-dependent band structure of FGT leading to $T_{FM} >> T_{AFM}$. In contrast, a nonzero interlayer exchange coupling of directly vdW-integrated FGT layers suppresses the occurrence of the evident AFM spin alignment, particularly around the junction interface, resulting in much smaller PTMR ratios and gradual resistance changes with varying B.

In addition, other factors can contribute to diminishing the PTMR ratios. Structural disorder breaks the assumption of the transverse wavevector conservation in the process of tunneling and may sizably enhance transmission of the AFM spins in MTJ, thus reducing TMR. Magnetic disorder, such as noncollinear spins at the interface between twisted FGT layers, also significantly reduces TMR due to spin mixing in the process of tunneling. The same mechanism of TMR reduction can be caused by spin–orbit interaction. Finally, nonstoichiometry of the FGT may also play an important role. Effectively, it can cause electron or hole doping shifting the Fermi energy from the value found for stoichiometric FGT.

3.5. Comparison to Other TMR (Like) Structures Using FGT Electrodes

A comparison chart of vdW TMR (like) structures using two FGT electrodes (except for the case of twisted bilayer CrSBr) is presented in **Figure 6**. Among these, the nontwisted FGT/hBN/FGT vdW junction structure reported the highest TMR value of ≈300% to date.[30] Incorporating vdW semiconductor spacer layers (e.g., GaSe,[34] $MoSe_2$[30]) into the nontwisted TMR junctions also achieved TMR values ranging from ≈10% to ≈200%. On the other hand, only the present vdW gap structure and ref. [35], which is close to the present structure, feature the twisted homojunctions, demonstrating the PTMR behaviors. However, the latter structure reported the lowest TMR-like (plateau-like) value of ≈0.07% at θ_t, ≈90°. These results highlight the substantial advantage of the present twisted homojunction, which achieves a PTMR value of ≈14% at θ_t ≈45° by applying V_{bg} as high as +45 V even without the need for spacer layers. Beyond FGT electrodes, twisting bilayers of CrSBr, a 2D antiferromagnet, have recently exhibited a TMR value as high as ≈900% at θ_t, ≈10° under B = 0.[38] However, these homojunctions are composed of insulating layers of CrSBr, where tunneling arises inherently from the nature of these layers. In contrast, our results involve no insulating layers, emphasizing a distinct experimental approach.

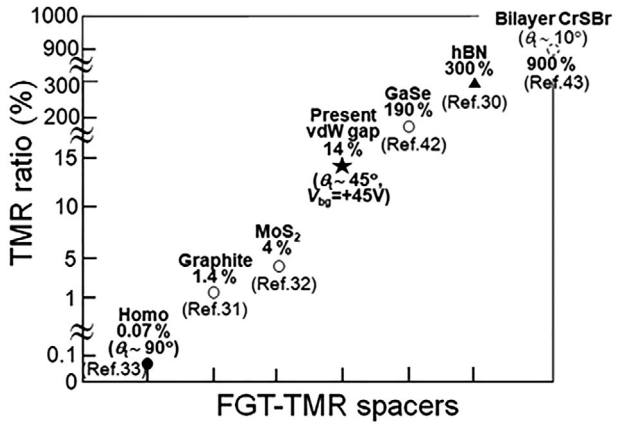

Figure 6. A comparison chart of vdW TMR (like) structures utilizing two FGT electrodes, except for the case of twisted bilayer CrSBr, a 2D antiferromagnet. The FGT/hBN/FGT device represents a conventional nontwisted vdW TMR structure, whereas GaSe, MoS_2, and graphite vdW spacers are noninsulating in these nontwisted TMR structures. Notably, only the present vdW-gap and another homojunctions (33) possess twisted vdW integration structures with a defined θ_t.

4. Conclusions

In conclusion, we have assembled vdW homojunctions of the thin-magnetic FGT flakes with large θ_t ranging from 0° to 90°, without inserting tunnel barriers. These vdW homojunctions have exhibited PTMR effect with the ratio highly sensitive to the θ_t values: peaking at ≈14% at θ_t = 45° and V_{bg} of +45 V and nearly vanishing at θ_t = 60°. This effect implied that the Δ_g between twisted thin magnetic layers can magnetically decouple them and provide conditions for spin-dependent tunneling. The θ_t served as a control parameter of PTMR involving two mechanisms: the interlayer exchange coupling and symmetry-controlled spin-dependent transmission across the Δ_g, depending on the magnitude of lattice mismatch which causes the AFM spin alignment. While the measured PTMR ratios are still small from the perspective of device applications, our previous theory[29] predicts TMR ratios larger than 1000% for the nontwisted FGT/vacuum gap/FGT TMR structure. This indicates that the PTMR ratios can be enhanced by optimizing the twisted structures and measurement conditions (e.g., by controlling the uniformity and reproducibility of the large Δ_g, reducing the constant currents for TMR measurements, encapsulating the twisted homojunction into vdW hBN layers, and inserting vdW spacers between the largely twisted magnetic layers) further. Our findings reveal the interplay between twistronics and spintronics, and pave the way for the exploration of AFM spin-dependent phenomena in largely twisted vdW heterostructures and their potential application in spintronic devices.

5. Experimental Section

vdW-integrated and twisted two thin FGT flakes with various θ_t are formed using the following method. Initially, thin FGT flakes are mechanically exfoliated from a bulk sample using the Scotch tape method. Subsequently, the upper and lower layers of the flake are separated into two copies and transferred to two different polydimethylsiloxane (PDMS) sheets, while maintaining alignment between the edges of the Scotch tapes and the

two individual PDMS sheets in parallel (Figure S1A, Supporting Information). The lower flake is attached onto one of prefabricated two-terminal Au/Ti electrodes on a SiO_2/Si substrate, ensuring alignment between the edges of the PDMS and the Si substrate in parallel. Next, the upper layers from another PDMS sheet are quickly vdW integrated onto a portion of the lower layers and another electrode at various θ_t using a 2D heterostructure transfer system (HQ Graphene Co.), resulting in the twisted junction area (Figure S1B, Supporting Information). Finally, each sample is covered by hexagonal boron nitride (hBN) layers. All processes are carried out in a glovebox with Ar-gas atmosphere

Supporting Information

Supporting Information is available from the Wiley Online Library or from the author.

Acknowledgements

The authors thanked S. Murakami, Y. Yamamoto, T. Ando, K. Nomura, T. Koretsune, S. Ozawa, C. Lee, L. Holleis, A. Young, J. G. Park, A. H. Macdonald, and P. Kim for their technical contributions, fruitful discussions, and encouragement. The work at the Aoyama Gakuin University was partly supported by the Aoyama Gakuin University Research Institute grant program for the creation of innovative research. Work at the University of Tokyo was partly supported by JSPS KAKENHI (Grant Nos. JP23H00174 and JP23H05443) and by JST, CREST (Grant No. JPMJCR20B5, Japan) for S.M. and JST-CREST (Nos. JPMJCR20C1 and JPMJCR20T2), Grant-in-Aid for Scientific Research (Nos. JP19H05600 and JP22K18686) and Grant-in-Aid for Transformative Research Areas (No. JP22H05114) from JSPS KAKENHI, MEXT Initiative to Establish Next-generation Novel Integrated Circuits Centers (X-NICS) (No. JPJ011438), Japan, and Institute for AI and Beyond of the University of Tokyo for T.K. and E.S.K.W. and T.T. acknowledged support from the JSPS KAKENHI (Grant Nos. 20H00354, 21H05233, and 23H02052) and World Premier International Research Center Initiative (WPI), MEXT, Japan. The research work at University of Nebraska-Lincoln was primarily supported by the Grant No. DE-SC0023140 funded by the U.S. Department of Energy, Office of Science, Basic Energy Sciences (K.S., N.A.S., and E.Y.T.). K.D.B. acknowledged support from the National Science Foundation through Grant Nos. DMR-1916275 and DMR-2324203 and from a UNL Grand Challenges catalyst award entitled Quantum Approaches Addressing Global Threats.

Conflict of Interest

The authors declare no conflict of interest.

Data Availability Statement

The data that support the findings of this study are available in the Supporting Information of this article.

Keywords

large angle twistronics, lattice mismatch, magnetic thin layers, magnetic tunnel junctions, van der Waals gaps

Received: August 4, 2024
Revised: December 24, 2024
Published online:

[1] Y. Cao, V. Fatemi, S. Fang, K. Watanabe, T. Taniguchi, E. Kaxiras, P. Jarillo-Herrero, *Nature* **2018**, *556*, 43.
[2] Y. Cao, V. Fatemi, A. Demir, S. Fang, S. L. Tomarken, J. Y. Luo, J. D. Sanchez-Yamagishi, K. Watanabe, T. Taniguchi, E. Kaxiras, R. C. Ashoori, P. Jarillo-Herrero, *Nature* **2018**, *556*, 80.
[3] M. Yankowitz, S. Chen, H. Polshyn, Y. Zhang, K. Watanabe, T. Taniguchi, D. Graf, A. F. Young, C. R. Dean, *Science* **2019**, *363*, 1059.
[4] L. Wang, E.-M. Shih, A. Ghiotto, L. Xian, D. A. Rhodes, C. Tan, M. Claassen, D. M. Kennes, Y. Bai, B. Kim, K. Watanabe, T. Taniguchi, X. Zhu, J. Hone, A. Rubio, A. N. Pasupathy, C. R. Dean, *Nat. Mater.* **2020**, *19*, 861.
[5] X. Lu, P. Stepanov, W. Yang, M. Xie, M. A. Aamir, I. Das, C. Urgell, K. Watanabe, T. Taniguchi, G. Zhang, A. Bachtold, A. H. MacDonald, D. K. Efetov, *Nature* **2019**, *574*, 653.
[6] M. Xie, A. H. MacDonald, *Phys. Rev. Lett.* **2020**, *124*, 097601.
[7] K. Hejazi, C. Liu, H. Shapourian, X. Chen, L. Balents, *Phys. Rev. B* **2019**, *99*, 035111.
[8] A. L. Sharpe, E. J. Fox, A. W. Barnard, J. Finney, K. Watanabe, T. Taniguchi, M. A. Kastner, D. Goldhaber-Gordon, *Science* **2019**, *365*, 605.
[9] N. Bultinck, S. Chatterjee, M. P. Zaletel, *Phys. Rev. Lett.* **2020**, *124*, 166601.
[10] Y.-H. Zhang, D. Mao, T. Senthil, *Phys. Rev. Res.* **2019**, *1*, 033126.
[11] M. Xu, H. Ji, L. Zheng, W. Li, J. Wang, H. Wang, L. Luo, Q. Lu, X. Gan, Z. Liu, X. Wang, W. Huang, *Nat. Commun.* **2024**, *15*, 562.
[12] M. Xu, H. Ji, M. Zhang, L. Zheng, W. Li, L. Luo, M. Chen, Z. Liu, X. Gan, X. Wang, W. Huan, *Adv. Mater.* **2024**, *36*, 2313638.
[13] Y. Yang, J. Li, J. Yin, S. Xu, C. Mullan, T. Taniguchi, K. Watanabe, A. K. Geim, K. S. Novoselov, A. Mishchenko, *Sci. Adv.* **2020**, *6*, eabd3655.
[14] O. Can, T. Tummuru, R. P. Day, I. Elfimov, A. Damascelli, M. Franz, *Nat. Phys.* **2021**, *17*, 519.
[15] S. Y. F. Zhao, X. Cui, P. A. Volkov, H. Yoo, S. Lee, J. A. Gardener, A. J. Akey, R. Engelke, Y. Ronen, R. Zhong, G. Gu, S. Plugge, T. Tummuru, M. Kim, M. Franz, J. H. Pixley, N. Poccia, P. Kim, *Science* **2023**, *382*, 1422.
[16] P. A. Volkov, S. Y. Frank Zhao, N. Poccia, X. Cui, P. Kim, J. H. Pixley, **2023**, arXiv:2108.13456v1.
[17] H. Xie, X. Luo, G. Ye, Z. Ye, H. Ge, S. H. Sung, E. Rennich, S. Yan, Y. Fu, S. Tian, H. Lei, R. Hovden, K. Sun, R. He, L. Zhao, *Nat. Phys.* **2022**, *18*, 30.
[18] Y. Deng, Y. Yu, Y. Song, J. Zhang, N. Z. Wang, Z. Sun, Y. Yi, Y.i Z. Wu, S. Wu, J. Zhu, J. Wang, X. H. Chen, Y. Zhang, *Nature* **2018**, *563*, 94.
[19] F. May, D. Ovchinnikov, Qi. Zheng, R. Hermann, S. Calder, B. Huang, Z. Fei, Y. Liu, X. Xu, M. A. McGuire, *ACS Nano* **2019**, *13*, 4436.
[20] H. K. Gweon, S. Y. Lee, H. Y. Kwon, J. Jeong, H. J. Chang, K.-W. Kim, Z.i Q. Qiu, H. Ryu, C. Jang, J. W. Choi, *Nano Lett.* **2021**, *21*, 1672.
[21] M. Yang, Q. Li, R. V. Chopdekar, R. Dhall, J. Turner, J. D. Carlström, C. Ophus, C. Klewe, P. Shafer, A. T. N'Diaye, J. W. Choi, G. Chen, Y. Z. Wu, C. Hwang, F. Wang, Z. Q. Qiu, *Sci. Adv.* **2020**, *6*, eabb5157.
[22] Y. Wu, S. Zhang, J. Zhang, W. Wang, Y. L. Zhu, J. Hu, G. Yin, K. Wong, C. Fang, C. Wan, X. Han, Q. Shao, T. Taniguchi, K. Watanabe, J. Zang, Z. Mao, X. Zhang, K. L. Wang, *Nat. Commun.* **2020**, *11*, 3860.
[23] B. Ding, X. Li, Z. Li, X. Xi, Y. Yao, W. Wang, *NPG Asia Mater.* **2022**, *14*, 74.
[24] D. Chen, W. Sun, W. Wang, X. Li, H. Li, Z. Cheng, *J. Mater. Chem. C* **2022**, *10*, 12741.
[25] X. Hu, Y. Zhao, X. Shen, A. V. Krasheninnikov, Z. Chen, L. Sun, *ACS Appl. Mater. Interfaces* **2020**, *12*, 26367.
[26] D. Kim, S. Park, J. Lee, J. Yoon, S. Joo, T. Kim, K.-j. Min, S.-Y. Park, C. Kim, K.-W. Moon, C. Lee, J. Hong, C. Hwang, *Nanotechnology* **2019**, *30*, 245701.
[27] Y. Li, X. Hu, A. Fereidouni, R. Basnet, K. Pandey, J. Wen, Y. Liu, H. Zheng, H. O. H. Churchill, J. Hu, A. K. Petford-Long, C. Phatak, *ACS Appl. Nano Mater.* **2023**, *6*, 4390.

[28] R. Obata, M. Kosugi, Y. Oguchi, H. Sun, T. Kikkawa, C. Tomatsu, K. Suenaga, E. Saitoh, S. Maruyama, J. Haruyama, *Nanotechnology* **2024**, *35*, 475601.
[29] X. Li, J.-T. Lü, J. Zhang, L. You, Y. Su, E. Y. Tsymbal, *Nano Lett.* **2019**, *19*, 5133.
[30] K.-H. Min, D. H. Lee, S.-J. Choi, I.-H. Lee, J. Seo, D. W. Kim, K.-T. Ko, K. Watanabe, T. Taniguchi, D. H. Ha, C. Kim, J. H. Shim, J. Eom, J. S. Kim, S. Jung, *Nat. Mater.* **2022**, *21*, 1144.
[31] S. Albarakati, C. Tan, Z.-J. Chen, J. G. Partridge, G. Zheng, L. Farrar, E. L. H. Mayes, M. R. Field, C. Lee, Y. Wang, Y. Xiong, M. Tian, F. Xiang, A. R. Hamilton, O. A. Tretiakov, D. Culcer, Y.-J. Zhao, L. Wang, *Sci. Adv.* **2019**, *5*, eaaw0409.
[32] H. Lin, F. Yan, C. Hu, Q. Lv, W. Zhu, Z. Wang, Z. Wei, K. Chang, K. Wang, *ACS Appl. Mater. Interfaces* **2020**, *12*, 43921.
[33] Y. Su, X. Li, M. Zhu, J. Zhang, L. You, E. Y. Tsymbal, *Nano Lett.* **2021**, *21*, 175.
[34] W. Zhu, Y. Zhu, T. Zhou, X. Zhang, H. Lin, Q. Cui, F. Yan, Z. Wang, Y. Deng, H. Yang, L. Zhao, I. Zutic, K. D. Belashchenko, K. Wang, *Nat. Commun.* **2023**, *14*, 5371.
[35] J. Kim, S. Son, M. J. Coak, I. Hwang, Y. Lee, K. Zhang, J.-G. Park, *J. Appl. Phys.* **2020**, *128*, 093901.
[36] T. Song, X. Cai, M. W.-Y. Tu, X. Zhang, B. Huang, N. P. Wilson, K. L. Seyler, L. Zhu, T. Taniguchi, K. Watanabe, M. A. McGuire, D. H. Cobden, D. Xiao, W. Yao, X. Xu, *Science* **2018**, *360*, 1214.
[37] H. H. Kim, B. Yang, T. Patel, F. Sfigakis, C. Li, S. Tian, H. Lei, A. W. Tsen, *Nano Lett.* **2018**, *18*, 4885.
[38] Y. Chen, K. Samanta, N. A. Shahed, H. Zhang, C. Fang, A. Ernst, E. Y. Tsymbal, S. S. P. Parkin, *Nature* **2024**, *632*, 1045.
[39] J. G. Checkelsky, M. Lee, E. Morosan, R. J. Cava, N. P. Ong, *Phys. Rev. B* **2008**, *77*, 014433.
[40] C.-G. Duan, J. P. Velev, R. F. Sabirianov, Z. Zhu, J. Chu, S. S. Jaswal, E. Y. Tsymbal, *Phys. Rev. Lett.* **2008**, *101*, 137201.
[41] S. Y. Park, D. S. Kim, Y. Liu, J. Hwang, Y. Kim, W. Kim, J.-Y. Kim, C. Petrovic, C. Hwang, S.-K. Mo, H.-J. Kim, B.-C. Min, H. C. Koo, J. Chang, C. Jang, J. W. Choi, H. Ryu, *Nano Lett.* **2020**, *20*, 95.
[42] K. D. Belashchenko, E. Y. Tsymbal, M. van Schilfgaarde, D. A. Stewart, I. I. Oleynik, S. S. Jaswal, *Phys. Rev. B* **2004**, *69*, 174408.
[43] K. D. Belashchenko, E. Y. Tsymbal, in *Spintronics Handbook: Spin Transport and Magnetism: Metallic Spintronics*, 2nd ed., Vol. *1*, (Ed: E. Tsymbal, I. Žutić), CRC Press, Boca Raton, FL, Chap. 13, **2019**, pp. 525–558.